Stability from subspace rotations and traveling waves

Tamal Batabyal[1,2,+], Scott L. Brincat[1,2,+], Jacob A. Donoghue[1,2], Mikael Lundqvist[1,2,3], Meredith K. Mahnke[1,2], Earl K. Miller[1,2*]

[1]The Picower Institute for Learning and Memory, Massachusetts Institute of Technology, Cambridge, MA 02139, USA
[2]Department of Brain and Cognitive Sciences, Massachusetts Institute of Technology, Cambridge, MA 02139, USA
[3]Division of Psychology, Department of Clinical Neuroscience, Karolinska Institute, Stockholm, Sweden
[+]These authors contributed equally
[*]Correspondence: ekmiller@mit.edu

Abstract

Cortical activity shows stability, including the ability to recover from disruptions. We analyzed spiking from the prefrontal cortex (PFC) of monkeys performing working memory tasks with mid-memory-delay distractions. Perturbation of cortex by events (a gaze shift or visual inputs) caused rotational dynamics in subspace that could return spiking to patterns similar to those before the perturbation. In fact, after a distraction, rotations were fuller when the task was correctly performed vs when errors were made. We found a direct correspondence between state-space rotations and traveling waves rotating across the surface of the PFC. This suggests a role for subspace rotations in cortical stability and a correspondence between subspace trajectories and traveling waves.

Introduction

The cortex is a highly interconnected network of nonlinear elements. As such, it should be prone to chaotic and unstable activity. Yet, the cortex manages to keep neural computations on track. Neural activity converges to stable sequences of states that produce consistent computations despite noise, variation, and disruption[1–6]. This consistency is reflected in subspace coding. The high-dimensional spiking of many neurons can be reduced to just a few meaningful dimensions. This indicates a great deal of coordination of spiking across neurons, emblematic of a highly stable

dynamic system. A variety of features of neurons and networks can work toward stability (e.g., anti-Hebbian plasticity, regulation of excitatory and inhibitory balance) [5,7–13].

One source of stability could be the neural dynamics themselves [5,14]. Subspace dynamics have a rotational component that is common across cortex and under a wide variety of conditions [15–21]. The rotations mean that spiking forms patterns that change in a stable and orderly fashion and often return to, or near, a previous state[15]. Hence, they could reflect and even help keep spiking patterns on the correct path of computation after deviations, a property of a stable system[5].

We used working memory for a test of stability. Memory maintenance can be disrupted by distractions, yet neural activity often, but not always, manages to recover and return to a pre-disruption state that restores focus on the task [22–27]. We examined activity from the prefrontal cortex of non-human primates (NHPs) performing two working memory tasks with a mid-memory delay distraction: a saccade or a visual distractor. We found that spiking activity showed rotational dynamics in subspace that were predictive of behavioral performance. We also found a correspondence between subspace rotations and traveling waves that rotated across the cortical surface.

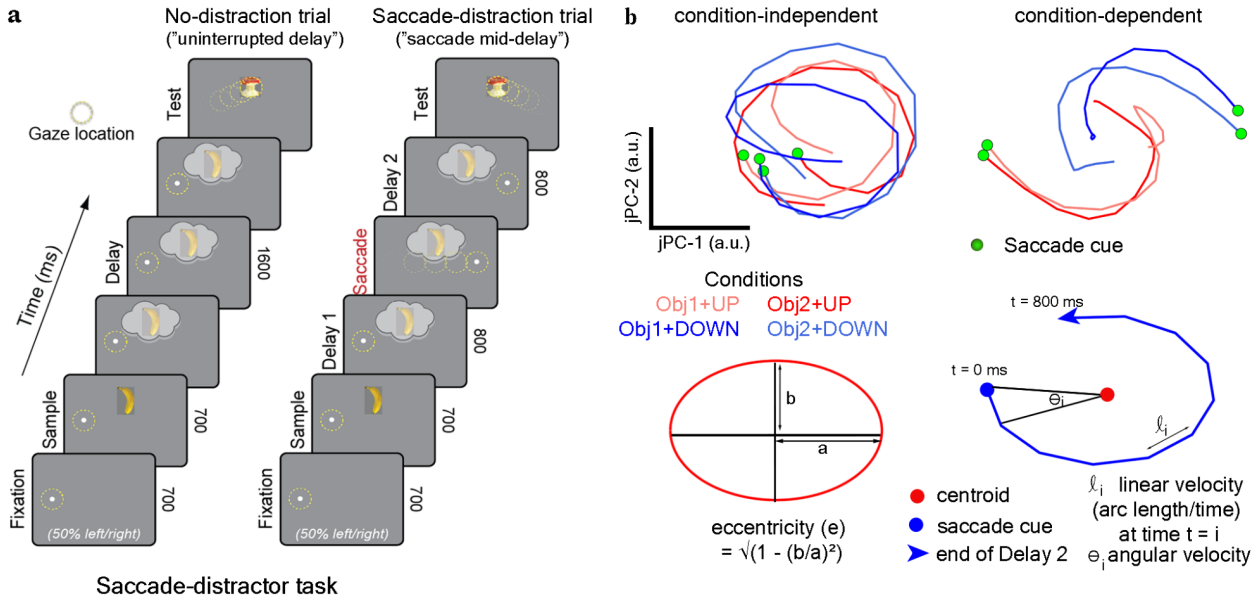

Figure 1. The saccade-distractor task and rotational dynamics. (**a**) A working memory task with a saccade in the middle of the delay. Subjects fixated to the left or the right of the center of the screen while a sample stimulus (randomly picked from one two images, Obj1, Obj2) was shown above or below the screen center. On half of the randomly-chosen trials a saccade instructed shift of gaze to the

opposite side of the screen. We focus on spiking after this saccade ("Delay 2"). (**b**) (top panel) Example of state-space (jPCA) rotations for four task conditions from Delay 2 in a single recording session. The condition-independent level captured all spiking whereas condition-dependent captured spiking specific to each of the four conditions. Rotations for each level are shown. The condition-dependent captured the variance due to object location (not object identity) with a 180-degree phase-shift between them. Rotational features included eccentricity, linear velocity and angular velocity.

Results

We used jPCA (rotational Principal Component Analysis) to capture rotations of spiking activity in subspace[15] (see Methods).

A disruptive saccade caused rotations in subspace

We first examined a visual-object working memory task that included (on half of randomly selected trials) a cued shift in gaze in the middle of the memory delay (Fig. 1a [28]). Neural activity was recorded from the dorsal lateral and ventral lateral PFC (dlPFC and vlPFC) from both hemispheres simultaneously. The gaze shift was designed to move the remembered location of the sample from one visual hemifield to the other. We previously found evidence that this transferred working memories from the corresponding (contralateral to the sample) "sending" hemisphere to the other "receiving" hemisphere[28]. Here, we use the saccade for a different purpose, as a distractor that could, and often did, disrupt working memory. Performance was higher on trials without the saccade-distractor (90.10 $\pm$ 0.004% correct) than trials with the distractor (80.33 $\pm$ 0.006% correct). Our main interest was how cortical activity "recovers" from the distractor. Thus, our analyses focus on the 800 ms from the saccade cue to the end of the memory delay ("Delay 2" in Fig. 1a).

We examined subspace rotations at two levels of specificity per Churchland et al [15]. Condition-independent spiking includes activity common across all task conditions (i.e., not specific to the different sample objects/locations, see Fig 1a). After the across-condition mean activity was subtracted, the remaining condition-dependent level captured rotations that specific to the different conditions. Fig. 1b shows details of how various metrics were calculated (also see Methods). We first examined data from correctly performed trials. Similar effects were observed in the dlPFC and vlPFC (Supplemental Fig. 1). Thus, for most analysis, we combined data across them.

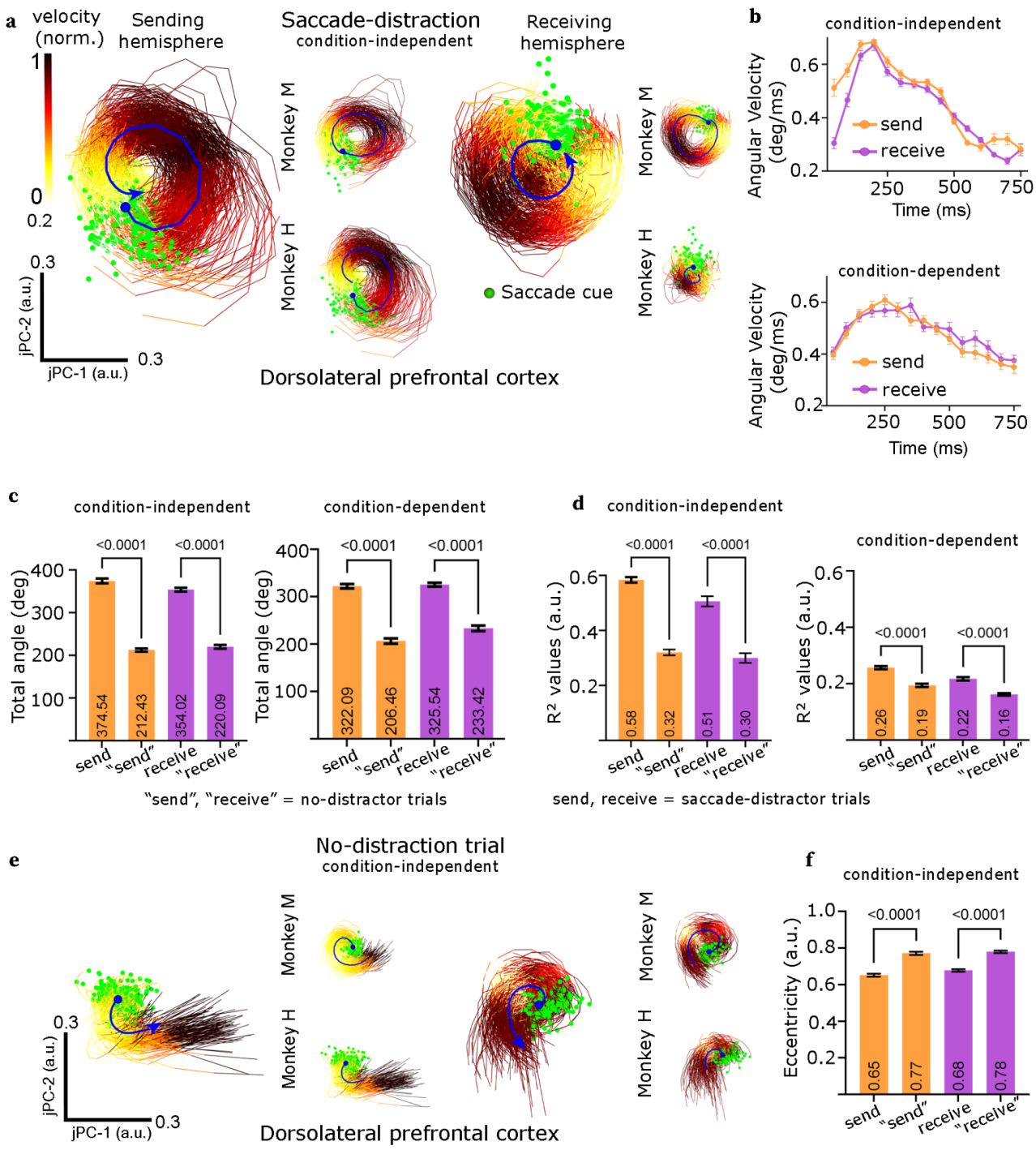

Figure 2. Saccades during working memory induce rotational dynamics

(**a**) Projections of neural data at the condition-independent level on the top two jPCs following the saccade (Delay 2) for all four conditions and for two NHPs (n = 55 sessions). Each trajectory was color-coded based on the normalized linear velocity (normalized arc length at each timestep). (**b**) Angular velocity over time after the cue to saccade. Rotations were fastest around the time of the saccade and then gradually slowed. (**c**) The total angle of rotation by the end of the memory delay. "Send" and

"receive" on no-distraction trials refer to the corresponding hemispheres on saccade-distraction trials. (**d**) R^2 estimates of fits of the jPCs to the data. At both levels, there was a better fit (more rotation) on trials with than without a saccade-distraction, $P < 0.0001$; both levels $t = 12.75, 9.77$, $df = 54$; paired t-tests; df = degrees of freedom. (**e**) Projections on the top two jPCs for the condition-independent level on no-distraction trials. (**f**) Trajectories in no-distraction trials had relatively large eccentricity (both hemispheres combined; mean $\pm$ s.e.m: no-distraction = 0.775 ± 0.007, distraction = 0.655 ± 0.007; $P < 0.0001$; $t = 14.6$, $df = 54$; paired t-test) values compared to saccade-distraction trials.

The saccade-distractor induced large-scale rotational dynamics in population spiking that was most prominent overall activity (i.e., the condition-independent level, Fig. 2a). The first two jPCs at the condition-independent level captured all the rotational dynamics. They explained about a third of the overall variance in spiking (condition-independent level: sending hemisphere = 0.33 ± 0.01, receiving hemisphere = 0.25 ± 0.02, see Supplemental Fig. 2 for the top 6 jPCs). The angular rotational velocity peaked around the time of the saccade and then gradually decreased over the remainder of the memory delay (Fig. 2b). At the condition-independent level, rotations were faster and peaked earlier in the sending hemisphere (Fig. 2b). This could be due to the earlier appearance of the sample in the corresponding visual hemifield (Fig. 1b). Note that trajectories, especially at the condition-independent level, completed up to a full 360° rotation (or more) by the end of the delay (Fig. 2c, sending hemisphere, average total rotation = 375 ± 5.8 degrees; receiving = 354 ± 4.56 degrees, mean $\pm$ s.e.m. solid orange and purple bars). Rotations were present but weaker at the condition-dependent level. The R^2 values showed a greater fit of rotational dynamics (top two jPCs) to the data at the condition-independent level than at the condition-dependent level (Fig. 2d). Correspondingly, rotations were fuller at the condition-independent than the condition-dependent level (Fig. 2c, e.g., sending hemisphere: 374 deg vs 322 deg, respectively).

For comparison, we examined the same time interval (latter half of the memory delay) on trials in which there was no distraction (no mid-delay saccade). There was still a rotational component without distraction, but it was weaker compared to saccade-distraction trials (Fig. 2e shows the condition-independent level). There was significantly less total rotation without distraction (Fig. 2c) and the jPCs showed a poorer fit to spiking (indicating a weaker rotational structure, Fig. 2d). The poorer rotational fit without distraction may be due to the elongated "tail" of each trajectory, indicating a lack of the full rotation seen after a distraction (Fig. 2a vs Fig. 2e). As a result, without a distractor, the trajectories showed less circularity and more eccentricity (Fig. 2f).

We confirmed the subspace rotations through a variety of controls. First, we randomly shuffled time-bins for all the conditions. This eliminated the rotations, as reflected in low R^2 values fitting data to the jPCs (condition-independent: $R^2 = 0.047 \pm 0.003$ for sending hemisphere; 0.027 ± 0.034 for receiving hemisphere, Supplemental Fig. 3). We also shuffled time-bins for just one condition chosen randomly, and then recomputed the jPCs[15]. This was repeated for all four conditions. Only the shuffled condition lost rotations, indicating that all the conditions contributed to the rotational structure (Supplemental Fig. 3). Sometimes a time-shifting pattern in data (i.e. different neurons with different spike latencies) can result in oscillatory jPCs, even if oscillatory dynamics are not actually in the data[29]. In these cases, all the jPCs show rotations. By contrast, in our case, the rotations were only evident in data projected onto the top two jPCs, not higher jPCs (Supplemental Fig. 2). Further, we confirmed rotations in the top two t-SNE dimensions (another dimensionality reduction method; see Supplemental Fig. 2), which does not have that issue. Finally, there was a ~90 degree phase difference between the projections, indicating a true rotation. Finally,

Rotations were more complete on correct than error trials

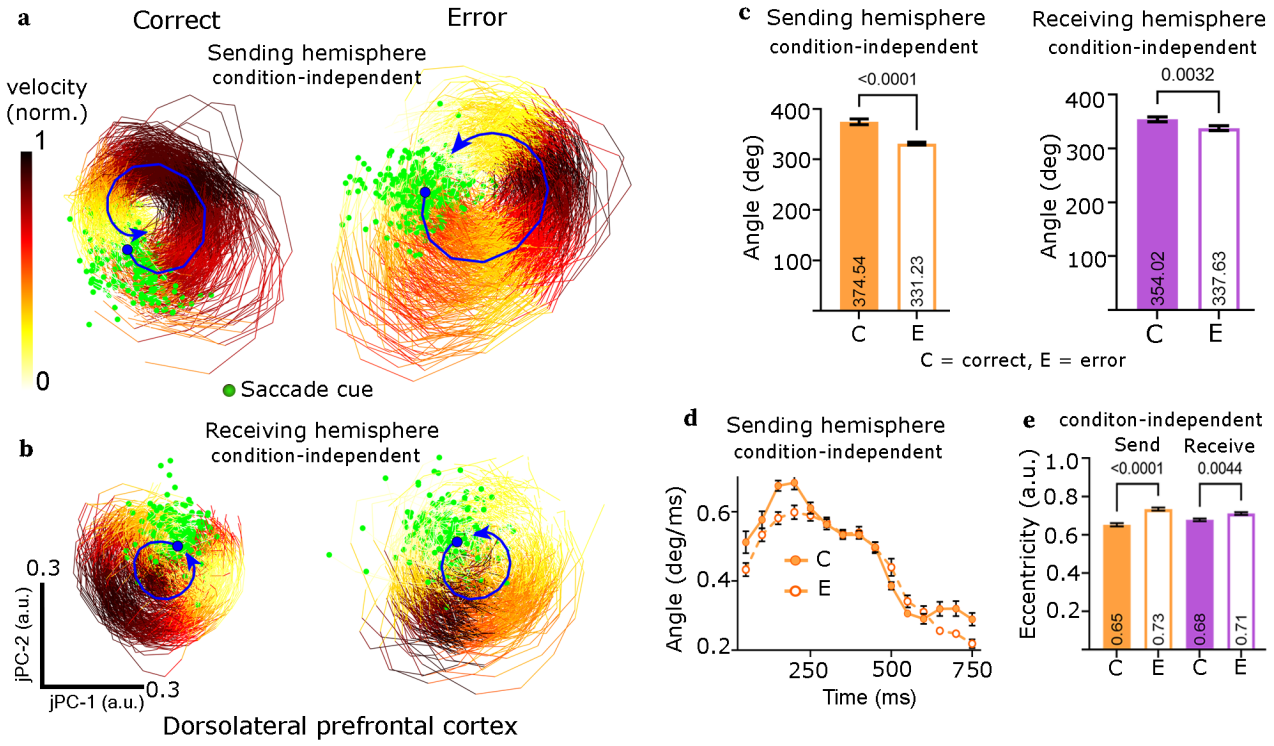

Figure 3. Behavioral effect of jPCA state-space rotations.

(**a**)-(**b**) The top two jPCs during Delay 2 for all the four conditions from dlPFC at the condition-independent level in cases of behaviorally correct and error trials. (**c**)-(**e**) Summary statistics combine the dlPFC and vlPFC, as above (**c**) Total angle of rotation for the sending (left panel) and receiving (right panel) hemispheres at the condition-independent level. Differences in angles between correct and error trials were observed in both hemispheres (sending hemisphere: $P < 0.0001$, $t = 7.56$; receiving hemisphere: $P = 0.0032$, $t = 3.08$; $df = 54$, paired t-test). (**d**) Angular velocity during correct and error trials at the condition-independent level. Just before and during the saccade (0-200 ms after saccade cue onset), angular velocity between correct and error trials was different ($P = 0.0065$, $t = 6.81$, $df = 3$, paired t-test). There was also a difference late in the delay (600-800 ms, $P = 0.027$, $t = 4.05$, $df = 3$, paired t-test). (**e**) Eccentricity of the correct and error trials at the sending and receiving hemispheres at the condition-independent level.

The saccade-distraction caused animals to make errors (causing a $9.77 \pm 0.007\%$ drop in correct choice, see above). On those trials, the trajectories at the condition-independent level failed to complete a full rotation before the end of the delay, unlike correctly performed trials (Fig. 3a,b). This was especially prominent in the sending hemisphere (331.22 ± 4.54 degrees on error trials versus 374.53 ± 8.75 degrees on correct trials, $P < 0.0001$, paired t-test, Fig. 3c). The angular velocities started slower on error trials (Fig. 3d). The error trial trajectories were less circular and more elliptical (Fig. 3e). The trajectories on correct trials tended to 'spiral in' towards the center late in the delay (Fig. 3a), which was not observed on error trials. For a fixed arc length, the closer the location of an arc to the center is, the larger angle it subtends. This spiraling in may be related to the rise in angular velocity late in the delay seen on correct bit not error trials (Fig. 3d). The receiving hemisphere also showed significant differences between correct error trials, albeit weaker than the sending hemisphere (Fig. 3b-e), as were rotational dynamics in general (see above).

Rotations were also induced by visual stimulation

We next asked whether visual distraction would induce the same dynamics as a saccade-distractor. We used another visual object working memory task (Fig. 4a). A visual distractor appeared in the middle of the memory delay. There were five different delay lengths (1, 1.41, 2, 2.83, and 4 s), randomly interleaved. The distractor appeared in the middle of the delay. We again began by focusing on the time that included distractor and remaining memory delay (Fig 4a, "Delay 2").

The visual distractor also caused rotations in subspace (Fig. 4b). Longer delays resulted in larger total rotations (Fig. 4c, correlation = 0.73 ± 0.12, $P < 0.0001$). The NHPs also had faster reaction times with longer delays. Thus, there was an inverse relationship between the degree of rotations

and the reaction time to the subsequent test stimulus (correlation = -0.4 ± 0.017, $P < 0.0001$, Fig. 4d).

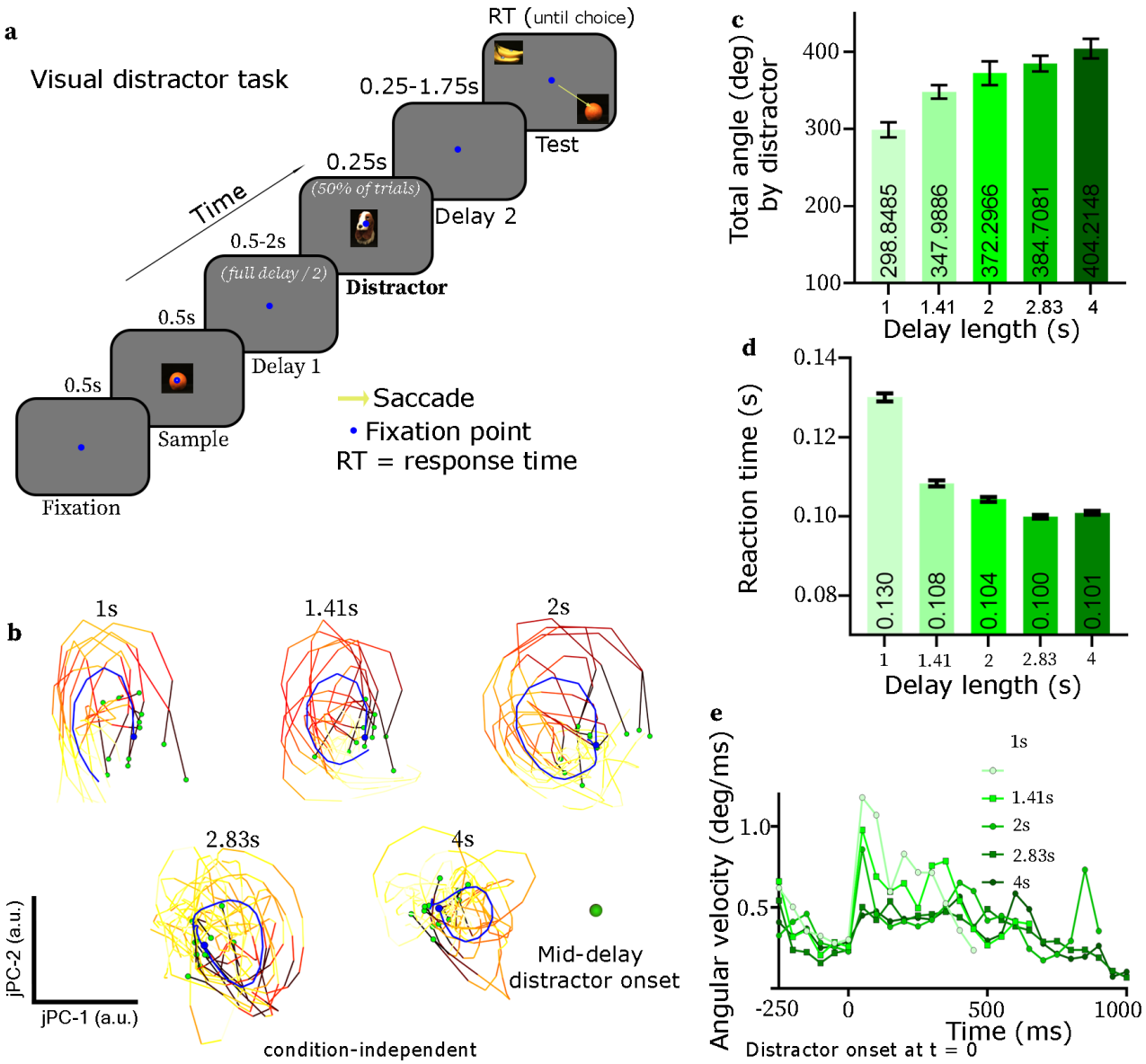

Figure 4. Rotational dynamics were also induced by visual distractors.
(**a**) A delayed-match-to-sample working memory task with a visual distractor. (**b**) Top two jPCAs (combined for both the left and right hemispheres) for five delay lengths at the condition-independent level. The length of the trajectory increased with the length of the delay. Color of a trajectory denotes the normalized linear velocity (arc length/time). (**c**) Total angle of rotation for each delay length at the condition-independent level. Longer delays resulted in longer rotations. (**d**) Reaction time (RT) for each delay length. RT was inversely correlated with the delay length. (**e**) Angular velocity of rotations. Angular velocity peaked within 200 ms after the distractor onset. Peak angular velocity was inversely correlated with the delay length ($r = -0.8 \pm 0.11$, $P < 0.0001$, t = -15.83, df = 5, t-test).

The rotational velocity showed a fast, then a slow profile following the visual distractor, peaking during the distractor at 200 ms (Fig. 4e), similar to that after the saccade-distractor (Fig. 2b). During that time (0-200 ms), the rotational velocity was fastest for the shortest delay (1 sec) and decreased in a graded fashion with increasing delay length (correlation = -0.8 ± 0.11, $P < 0.0001$).

The to-be-remember sample stimulus also produced rotations

Having found that distractors produced rotation, we wondered whether any event that perturbs cortex would also induce subspace rotations. Thus, we examined cortical responses to the to-be-remembered sample stimulus seen before the visual distractor. Like the distractor, the sample was a picture. We examined the interval from sample onset to the distractor ("Delay 1", Fig. 4a).

Like the visual distractor, the sample induced rotational dynamics in overall activity (Fig. 5a). However, the total angle of rotation (over the same duration) was significantly smaller to the sample (Fig. 5b, left) than to the distractor (Fig. 5b, right), at every delay length. This was true even though the relevant sample was presented for twice the duration (500 ms) than the irrelevant distractor (250 ms). This suggests that activity showed more recovery from the irrelevant distractor than the sample whose memory needed to be maintained.

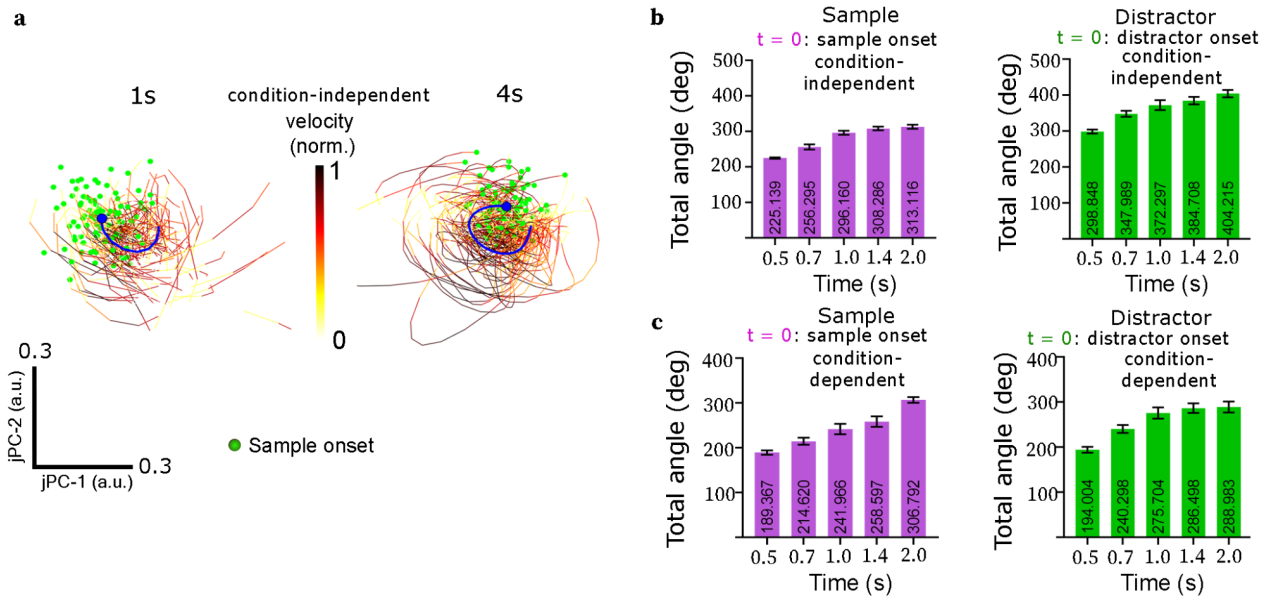

Figure 5. The sample stimulus also induced subspace rotations

(**a**) State-space trajectories induced by the sample stimulus at the condition-independent level for 1.41s and 4s delays. (**b**) Total angle at the condition-independent level for the sample vs distractor. At the

condition-independent level, the distractor caused more rotations than the sample at each time step (maximum P value = 0.0213, paired t-test).

Subspace rotations correspond with traveling waves rotating across the cortical surface

The observation of rotations in subspace raised the possibility of a relation to traveling waves, which often rotate in the cortex [30–36]. We observed traveling waves in local field potentials (LFPs) after the saccade-distractor (Fig. 6a and below) and after the visual distractor (see Supplemental Fig. 4). We identified traveling waves using generalized phase (GP) [34] of wideband-filtered LFP (Fig. 6b).

Spikes coupling to LFP phase during wave propagation (Fig. 6d; Rayleigh test for non-uniformity of circular data, $P < 0.0001$) and thus there were also traveling waves in spiking (Fig. 6c). The orderly change in principal direction of the waves (see Methods) for both LFP (Fig. 6a) and spike waves (Fig. 6c) was consistent with traveling waves. There were small changes in angular deviations over time indicative of a traveling wave (angular deviations; Fig. 6e, blue line). Shuffling the data across time (Fig. 6e, magenta line) or across electrode locations (Fig. 6e, red line, see also Supplemental Fig. 4) disrupted the wave as indicated by significantly increased angular deviations. Unlike the shuffled data, spiking activity also showed a significant decrease in angular deviation after the saccade ($P < 0.0001$, $t = 16.19$, $df = 15$, t-test with Welch's correction for variance; 48 ms before vs after the saccade-distractor), consistent with a traveling wave induced by the saccade (see Supplemental Figure 4 for the visual distractor.

This raised the possibility of a direct correspondence between traveling waves across cortex and subspace rotations. To test this, we removed subspace rotations from the spiking data by subtracting the first two jPC projections. This resulted in a significant increase in angular deviation indicating a loss of traveling wave structure in spiking (Fig. 6e, black line, difference in angular deviation = 31.32 ± 0.45, $P < 0.0001$, $t = 68.6$, $df = 97$, paired t-test; consistent difference over time: correlation coefficient = 0.53, $P < 0.0001$ (one-tailed)). To further test this, we sorted neurons based on their latencies to their peak spike rates following the saccade-distraction. The orderly offset in latencies also suggested a shifting spatio-temporal pattern of spiking (see also Supplemental Fig. 5). We next reconstructed the spike-rate data using only the top two jPCs (Fig. 6f,g) and ordered it in the same way as the original data. The similarity in patterns suggests a direct

relationship between subspace rotations (jPCs) and the orderly progression of spiking. The patterns were not present in the rest of the jPCs (3rd - 6th).

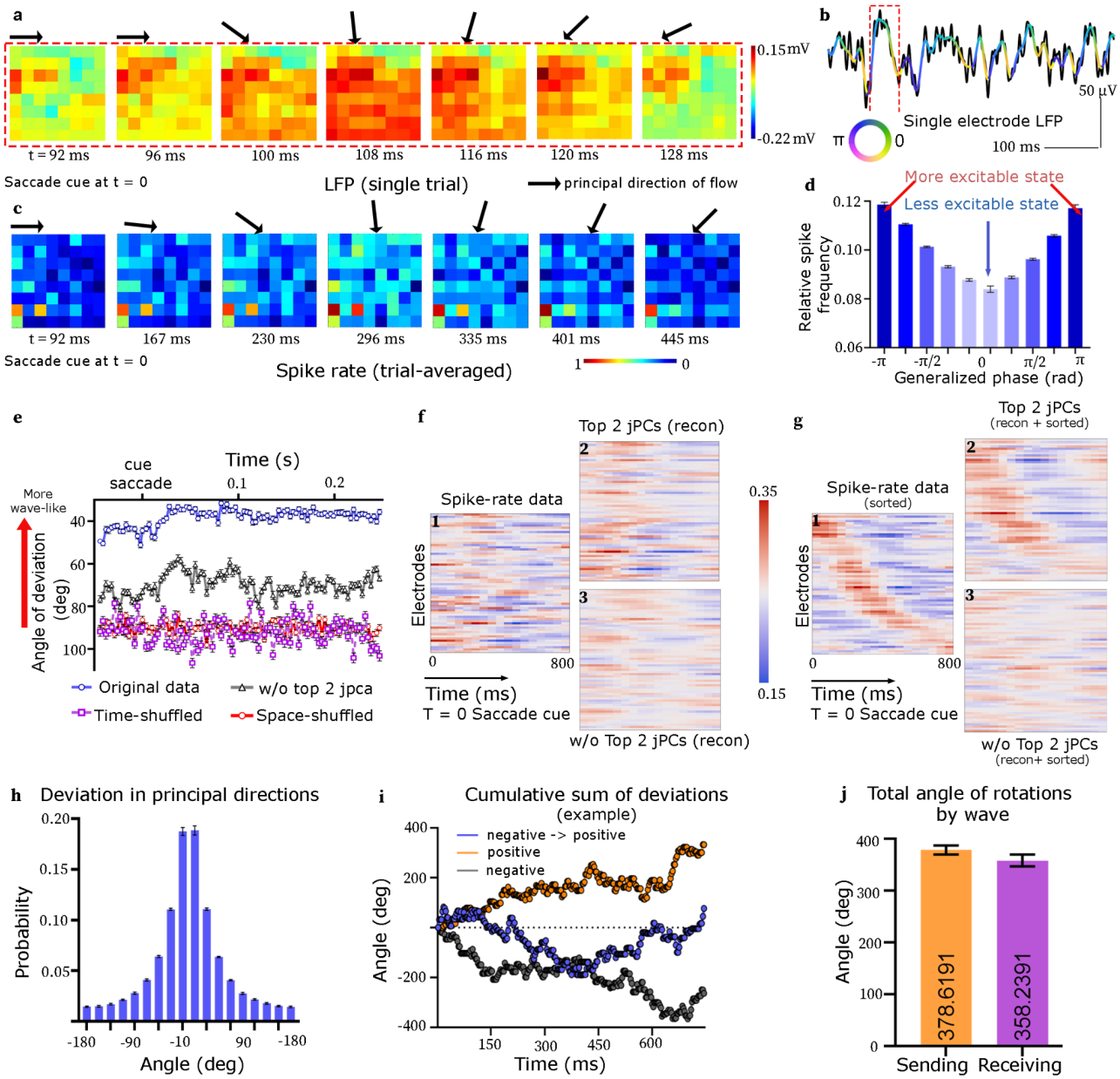

Figure 6. Traveling waves corresponded with jPCA rotations: Saccade-distractor task

(**a**) LFP voltages from an electrode array in the dlPFC of the sending hemisphere as a function of time during a single trial. The colorbar represents the voltage. The principal direction of flow of the activity is shown with black arrows. (**b**) Generalized phase of a wideband (5-40 Hz) filtered LFP signal from a single electrode. The striped red box in **(b)** is the same time as **(a)**. (**c**) A wave in the averaged spike-rate. (**d**) The distribution of spikes at different LFP phases in Delay 2 across sessions, [-π to π]. The relative

frequency peaked at ±π rads (Rayleigh test for non-uniformity of circular data, $P < 0.0001$), indicating coupling between spikes and LFPs. (**e**) Mean angular deviation of the principal direction of spike traveling waves across sessions (blue line). The same data is shown after subtracting the 1st two jPCs (black line) and after shuffling the data by time (magenta line) and electrode location (red line). (**f**) An example of spike-rate data in (**1**), the data only using the top 2 jPCs (**2**) and without the top two jPCs (**3**). (**g**) The raw data in (**f-1**) sorted by latency to peak spike rate (**1**). Data from the top 2 jPCs only using the same order **(2).** The data without the top 2 jPCs using the same order. It showed that the top two jPCs captured the dominant pattern present in the raw data. (**h**) Distribution of deviation of principal directions for spike traveling waves. Deviations in the range of [-35, 35] degrees comprised nearly 68% of the distribution. **(i)** Examples of cumulative rotations over time corresponding to three different types of wave dynamics using the central -35 to 35 degrees. 'Positive' and 'negative' correspond to counter-clockwise and clockwise directions of rotations, respectively. (**j**) Total rotations by the rotating wave in the sending and receiving hemisphere.

We found that the traveling waves rotated across the surface of the cortex. We divided the deviation in principle direction for the spike traveling waves arbitrarily into positive vs negative deviations relative to zero (no change, Fig. 6h). The deviations did not flip back and forth randomly between negative and positive. Instead, there were directional trends that remained consistent in either that remained consistent across time (yellow and gray, Fig. 6i) or only changed slowly (blue line, Fig 6i). The cumulative angular deviation over the delay period added to 360 degrees or more indicative of a rotational movement and similar to the full rotations seen in subspace (Fig. 6j).

Discussion

Rotations in subspace reflect an organized progression of spiking patterns. We found that spiking activity in the prefrontal cortex undergoes rotations after perturbation by an event, whether that event was a distraction or to-be-remembered object. This returned spiking to patterns similar to those before perturbation. As such, these dynamics could correspond to a crucial brain function: Dynamic Stability [5]. Despite variation and noise in neural activity, the brain has to converge to a stable, reproducible sequence of states and return to the proper "track" when perturbed[5,37,38]. In fact, we found fuller rotations after a distractor when the task was correctly performed. We also found evidence that rotations in subspace corresponded with rotating travel waves across the surface of cortex, a possible link between traveling waves and neural computation in subspace.

Rotational subspace dynamics seem to be a common motif in the cortex. They have been reported in the motor cortex, premotor cortex, somatosensory cortex, visual cortex, parietal, and prefrontal

cortices [15,17,19,39,39–48]. The rotations, in essence, return spiking to a state near to that before the perturbation that induced them, much as working memory representations are lost and then reinstated [22,23,25] . This is not an outcome of a system with chaotic dynamics, which amplifies noise and disruptions [5,49]. Instead, it is a signature of contracting dynamics [6]. Contracting dynamics make the brain less susceptible to perturbation, noise, and initial conditions. Thus, subspace rotational dynamics could be a general mechanism for achieving stability in the cortex. The rotational dynamics could arise from different motifs of anatomical connectivity[15,42,47].

Rotational subspace dynamics does not necessarily mean a complete “reset” back to a previous state. Mathematically, the difference between the final state and the initial state fell into the null space of the first two jPCA axes after the rotation. This means that the final state differs from the initial state by a non-rotational component. In other words, the end state could be further down the “correct” computational path. In fact, the rotations were not as full after the to-be-remembered samples than after the to-be-ignored visual distractors. This could reflect retention of information about the sample. But we cannot discount the explanation that the samples and distractors were presented for different durations (500 vs 250 ms). However, the samples were presented for twice as long as the distractors, which a priori might be expected to produce more, not less, rotation.

Rotations in general suggest push-pull type mechanisms. The jPC axes are derived by estimating a skew-symmetric matrix, a functionally asymmetric influence between the axes. One dimension (one jPC axis) exerts a positive influence on the other which negatively influences the first [15]. Thus, the disruption “pushes" the neural state away from the prior trajectory, but then compensatory dynamics “pull” it back towards the original trajectory. We note that push-pull rhythmic dynamics has been widely reported between lower and higher frequency oscillations in cortex [53–55]. This raised the possibility that the rotations in subspace have a oscillatory dynamic.

The subspace rotations seemed to correspond to travel waves that rotated across the surface of the cortex. This is consistent with previous work linking rotational subspace dynamics to sequential neural activation[56]. Like subspace rotations, rotating traveling waves are common across cortex [32,33,35,36,56–61]. Traveling waves speed up when a memory delay is shorter[62], a property we also found in subspace rotations.

Traveling waves have properties useful for a variety of functions [30,31,34,63–65], including regulating attentional scanning and tracking time and recent network activity [66–69]. Visual targets are better

detected when traveling waves in the cortex are better organized. Rotating travel waves, in particular, have useful properties for neural computation[30]. This, in addition to stability, may explain why they are common in the cortex [35,36]. A rotating wave has different speeds of propagation along the radius of its arm. This influences network activity in a graded fashion. This creates a structure of time differences with smaller differences closer to the center of rotation. The gradient due to rotating travel waves has been suggested as a mechanism to control spike-dependent plasticity [31,32]. Changing the center of the rotation adds an additional level of control[36,70]. Spatial Computing shows how such ordered spatiotemporal changes in activity could underlie control of neural computation [53]. The correspondence between rotations in subspace and traveling waves raises the possibility that neural computations are controlled by traveling waves.

Methods

Behavioral paradigm

We employed two visual working memory tasks. In both tasks, there was a distraction in the middle of the memory delay, either a cued shift in gaze or an irrelevant visual distractor.

The saccade-disruptor task (monkeys M and H) is shown in Fig. 1a. The trial began with 700 ms of central fixation. Then, a sample object appeared for 700 ms to the right or left visual hemifield, either 3.4 degrees above or below the center of the screen. The sample was one of two objects from a commercial photo-library (Hemera Photo-Objects). The task required memory of the sample object and location over a memory delay period of 1600 ms. On 50% of the trials, there was an a gaze shift was instructed by moving the fixation point across the vertical midline to the opposite side (“saccade”, Fig 1a). This gaze shift moved the remembered retinotopic location of the sample, being held during the working memory delay, to the opposite visual hemifield. At the end of the delay, a test object appeared for 400 ms. The monkeys were required to saccade to it if it did not match the remembered sample in either object identity or upper/lower location. If the test was identical to the sample, they withheld response. Then, after a 100 ms blank period, a nonmatching test object was always shown, which required a saccade. Response to the non-match was rewarded with juice, followed by a 3.2 s inter-trial interval.

In another task, an NHP trained on delayed-match-to-sample task with a visual distractor mid-delay (Fig. 3a). The trial began with 500 ms of central fixation. A sample object appeared for 500 ms at the center of the screen, followed by a delay period. The duration of the delay was randomly selected from a set ([1s, 1.41s, 2s, 2.83s, 4s]). In a random 50% of trials, a distractor object (from a different set of objects as the sample) was presented for 250 ms at the middle of the delay. During the test period, the NHP was allowed to freely saccade between test objects and then indicate the final choice by holding fixation on it for 1s.

All the stimuli were displayed on an LCD monitor. An infra-red eye-tracking system (Eyelink 1000 Plus,SR-Research Ontario, CA) continuously monitored eye position at 1 kHz.

Electrophysiological data collection

The subjects were chronically implanted in the lateral prefrontal cortex (PFC) with four 8×8 iridium-oxide “Utah” microelectrode arrays (1.0 mm length, 400 μm spacing; Blackrock microsystems, Salt Lake City, UT), for a total of 256 electrodes. Arrays were implanted bilaterally, one array in each ventrolateral and dorsolateral PFC in each hemisphere. Electrodes in each hemisphere were grounded and referenced to a separate subdural reference wire. LFPs were amplified, low-pass filtered (0-250 Hz), and recorded at 30 kHz. Spiking activity was amplified, filtered (2500-5000 Hz), and manually thresholded to extract spike waveforms. All threshold-crossing spikes on each electrode were pooled together and analyzed as multi-unit activity (MUA). We recorded 20 sessions from monkey M and 35 from monkey H for the saccade-distractor task, and 6 from monkey H for the visual-distractor task.

Quantification and statistical analysis

We examined neural responses to a saccade at the left and the right hemispheres separately in saccade trials. The results were pooled based on whether the sample was initially in the hemifield contralateral (sending) or ipsilateral (receiving) to the recorded hemisphere. The analysis was carried out using baseline-normalized spike-rate data during Delay 2 (800 ms) in saccade trials (Fig. 1a) and at an identical time period (800 ms) in no-saccade trials, as controls to the saccade trials. In the experiment with a mid-delay visual distractor, we performed analyses separately on each hemisphere and the results were pooled to perform statistical tests. For both experiments, individual sessions were treated as observations. All processing and computational analysis were

performed using MATLAB R2021b (Mathworks Inc., Natick, MA). The plots were generated using Prism (Graphpad software, MA).

Preprocessing

Spike-rates were computed by binning the spike timestamps in non-overlapping 50 ms windows. For the estimation of wave characteristics we also used bin-width of overlapping time windows of 45 ms. Spike-rates were square-root transformed that rendered the Poisson-like distribution of the spikes to an approximate normal distribution. LFPs were re-referenced offline to remove any common-source noise by subtracting off the mean across all electrodes in each array. Evoked potentials were removed by subtracting off the mean signals across trials within each condition in each hemifield. LFP power was log transformed to make its distribution approximately normal.

Mean activity analysis

To normalize out any differences in activity between the neurons in all the task-conditions, the spike-rates were z-scored to the fixation baseline. We take a 500 ms time window before the sample onset and computed spike-rates. The spike-rates were then mean-pooled separately for each neuron and for each condition for each array location. The mean and standard deviation across all within-conditioned trials were computed. For each neuron and condition, these statistics were then used for z-scoring spike-rates across all trials. We used z-scored spike-rates for further analysis.

Subspace coding that captures rotational dynamics

To identify the population-level oscillatory dynamics from spiking data, jPCA was used. Trial-averaged z-scored spike-rate data with dimensions as (neuron X timebin) was considered as input to jPCA. For each neuron i, we computed the range of its spike-rate along time and performed soft-normalization as

$$\widehat{s_i}(t) = s_i(t)/(range(s_i) + \theta);\ \theta = const., i = \{1,2,\ldots,N\}, N = number\ of\ neurons$$

Soft-normalization rendered the neural responses to have a similar range of firing activity. We used 0.5 as the constant in all of our analysis. Most of our analysis focused separately on those aspects of neural responses that were common to and that differed across conditions. We tagged them as condition-independent and condition-dependent respectively. In condition-dependent analysis, the across-condition mean was subtracted off the data from each condition.

At each level, the soft-normalized data were put together or stacked to compile an augmented data matrix, $= [X_1\ X_2 \ldots X_M]$; $X \epsilon R^{N \times Mt}$. Here, M is the number of conditions; N is the number of neurons; t is the number of time bins. X was then projected onto the subspace of its top six principal components (PCs), rendering X to a low dimensional data X_{low} of size 6 X Mt. Six principal components preserved at least 90% of the data variance.

To capture rotational dynamics in the normalized data, we computed jPCA [15]. jPCA is a dimensionality reduction algorithm that finds the strongest rotational components of the neural activity. To compute jPCA, an antisymmetric state-space matrix, $D_{skew}\ \epsilon R^{6 \times 6}$ was computed by fitting a linear model, $\frac{dX_{low}}{dt} = D_{skew}X_{low}$. Quality of the fit was assessed by R^2 values. R^2 denotes the ability to linearly predict $\frac{dX_{low}}{dt}$ from X_{low}, which, in turn, indicates the strength of rotational dynamics in neural responses. By definition, D_{skew} has imaginary eigenvalues, capturing rotational dynamics. The two eigenvectors of D_{skew}, U_1 and U_2 corresponding to the largest eigenvalue (one eigenvalue is the conjugate of the other) formed a plane that captured the rotational dynamics with highest angular velocity. U_1 and U_2 were complex-valued vectors. The jPCs were obtained as $jPC_1 = (U_1 + U_2)/2$ and $jPC_2 = j(U_1 - U_2)$. The jPC projections were obtained as $[jPC_1;jPC_2]*X_{low}$. The jPCs spanned the identical subspace to that of the six PCs.
We computed jPCA on each session separately. In each session, the jPCA algorithm yielded four projections corresponding to four task conditions ((obj1,UP), (obj1,DN), (obj2,UP), (obj2,DN)) in the hemifield-swap data. To obtain the average trajectory of all the sessions in a given hemisphere at the condition-independent level, we computed an average trajectory of all the conditions. We took the average trajectory at session 1 as a reference. We obtained the best rotation, say Θ_i, to fit between the average trajectory of the ith session and the reference. The trajectories of individual conditions were then rotated by Θ_i to align with the reference. This procedure was used only for the visualization purpose (such as Fig. 2a). No computational analysis was performed on the rotated trajectories.

Subspace coding during variable delay

In the experiment with a mid-delay visual distractor, we computed jPCA in multiple phases. The shortest delay duration was 1s. To calculate the jPC projections for 500 ms from the distractor onset, we considered all five delay durations (1, 1.41, 2, 2.83, and 4 s) as conditions and analyzed the trajectories for the 1s delay only. To compute projections for larger delays, we progressively dropped one delay-length condition from the analysis. For example, to analyze dynamics for 700

ms after distractor onset, we only included delay-length conditions ≥ 1.41 s. Note that, within each delay-length condition, the sample was taken from a set of eight images. We pooled trials across all the samples and trial-averaged separately for each delay length.

Rotation feature computation

We computed the following features of rotational trajectories in our analysis; (1) angular velocity (= angle subtended by an arc over time at the center, (2) eccentricity (3) normalized jPCA variance (= fraction of data variance captured by the jPCA plane), and (4) R^2 values from D_{skew}. These features were computed separately for individual sessions. We then pooled all the features to compute the statistics required for the analysis.

Estimation of the center of a trajectory

Because of varying arc lengths in consecutive timesteps, a rotational trajectory was irregularly sampled in time. Prior to estimating the center, a trajectory was re-parameterized to have regularly spaced Q points on its trajectory. Each point has 2D coordinates in the plane formed by jPC_1 and jPC_2. The center of the trajectory was computer as $C = (x_c, y_c) = \frac{1}{Q}\sum_{i=1}^{Q} P(t_i)$; Here, $t_i \epsilon [0,1]$ is the new parameter of the trajectory P. We set Q= 50.

Estimation of eccentricity

To compute the eccentricity of a trajectory, we fit an ellipse using a Matlab code (https://www.mathworks.com/matlabcentral/fileexchange/3215-fit_ellipse). Using the estimated major (a) and minor (b) axes, the eccentricity e was computed as $e = \sqrt{1 - (b/a)^2}$. It is a real number lying in [0, 1], where zero indicates a perfect circle. It can be interpreted as a measure of homogenous changes in the firing rate over time.

Wave estimation

We employed an algorithm developed by Horn and Shunck [71,72] to measure optical flow, in order to detect and characterize traveling waves from noisy multi-unit recordings. Optical flow finds the apparent motion of objects in a visual scene. In our case, the object of interest is the neural activity. The optical flow algorithm takes a pair of consecutive frames and outputs a velocity vector field (flow field) that represents the direction and speed at each recording location. Here, a frame denotes the neural activity in the 2D recording array at an instant.

The wave detection algorithm occurs in three steps: 1. We computed maximum and minimum firing rates of all the neurons in the trial-averaged data in a session. The time interval, T, for wave estimation was selected. Let's assume the selected data be Z $\epsilon\ R^{neuron \times T}$. The data was then normalized in [0, 1] and scaled to [0, 255]. The data was then reshaped to the physical array dimension, which was $8 \times 8 \times T$ in our case. In case of missing data at an electrode in the array, we performed nearest-neighborhood interpolation to simulate the spike-rate data at that electrode. 2. Using the pre-processed data, we applied the "estimateFlow.m" MATLAB function to get velocity fields (v_x, v_y) in consecutive instants, where $v_x, v_y\ \epsilon\ R^{8\times8\times(T-1)}$. The direction of flow was determined by computing streamlines ("streamline.m" MATLAB function) of the flow field in each of the (T-1) frames. Streamlines are a family of curves whose tangent vectors form the velocity field of the flow. In short, a streamline is a path traced out by a massless particle as it moves with the flow. We used all possible starting locations (8×8) to generate all possible streamlines. We considered streamlines that visited at least half (= 4) of the recording electrodes. In the ith frame, let this set of selected streamlines be S_i. We denote the number of elements in the set, S_i as $|S_i|$. For each of the streamlines in S_i, we marked the recording electrodes and computed the vector average of (v_x, v_y) associated with the recording electrodes. This step provided a principal direction and magnitude (v_x^s, v_y^s) of flow along s. Using this, the principal direction of flow in the ith frame was given by

$$(f_x^i, f_y^i) = \left(\frac{1}{|S_i|}\sum_{s=1}^{|S_i|} v_x^s, \frac{1}{|S_i|}\sum_{s=1}^{|S_i|} v_y^s\right);\ i\ \epsilon\ [1,2,\ldots,T-1]$$

$$(f_{px}^i, f_{py}^i) = \left(\frac{f_x^i}{\sqrt{(f_x^i)^2 + (f_y^i)^2}}, \frac{f_y^i}{\sqrt{(f_x^i)^2 + (f_y^i)^2}}\right)$$

Examples of principal directions were given by black arrows in Fig. 6c.

In short, the principal direction of flow (neural activity) between two frames is the direction of the dominant flow between two instants. Note that we did not compute the unit vector of (v_x^s, v_y^s). This way, (f_x^i, f_y^i) is an average of (v_x^s, v_y^s) across all s, weighted by the magnitude of (v_x^s, v_y^s). This action will bias (f_x^i, f_y^i) towards a subset of streamlines (s), which correspond to the dominant flow.

A traveling wave has a spatio-temporal organization. The spatial organization was encoded in the principal direction. We evaluated how the principal direction was changing over time to examine the temporal organization of the wave. We computed the dot product of (f_{px}^i, f_{py}^i) in consecutive frames to estimate the deviation of the principal flow direction over time. Traveling waves result in a

relatively small deviation of the principal angle in consecutive frames, due to consistent or slowly changing temporal structure. In the absence of traveling waves, successive principal angles will be random, thus resulting in a large deviation (~90 degrees) of the principal angle in consecutive frames (Fig. 6e).

LFP phase-spike coupling

To find the LFP phase - coupling, we computed the generalized phase (GP), which captured the dominant fluctuation of LFP on each electrode at each point of time.This estimation of phase (GP) of this fluctuation was not contaminated by very low frequency or high frequency intrusions. As noted in [34], the LFP signal was channeled through a wideband [5, 40 Hz] filter before the computation of GP. We computed the GP of LFP at each electrode location. No averaging of LFP was performed. We sampled the GP at the times of spikes on each electrode. We pooled all the sampled GP values from all the trials in each session and computed a histogram with equally-spaced 10 bins of phase values ranging $-\pi$ to π. The histogram was then normalized to obtain a probability distribution in each session. We pooled the distributions in all sessions and all animals, and averaged them to get the LFP phase to spike coupling.

Hypotheses testing

In all hypothesis tests, we treated each session as an observation. We used paired t-test (session-wise paired) in the majority of our analysis. For observations with unequal variance, we used t-test with Welch's correction. We used the Rayleigh test for circular uniformity, used for testing the effect of LFP phase-spike coupling. To test with more than two variables, we used one-way ANOVA in which an F-statistic was computed. All tests were subjected to Bonferroni's correction for multiple comparisons.

Data availability

The data that support the findings of this study are available from the corresponding author (E.K.M.) upon reasonable request.

Code availability

Data analysis was performed using MATLAB R2021b (Mathworks Inc., Natick, MA).

External toolboxes - jPCA (https://www.dropbox.com/sh/2q3m5fqfscwf95j/AAC3WV90hHdBgz0Np4RAKJpYa?e=1&dl=0), CircStat version 1.21.0.0 (https://www.mathworks.com/matlabcentral/fileexchange/10676-circular-statistics-toolbox-directional-statistics), fit_ellipse (https://www.mathworks.com/matlabcentral/fileexchange/3215-fit_ellipse) were used. Key built-in MATLAB functions, such as estimateFlow.m and streamline.m were used for wave estimation.

References

1. Spaak, E., Watanabe, K., Funahashi, S. & Stokes, M. G. Stable and Dynamic Coding for Working Memory in Primate Prefrontal Cortex. *J. Neurosci.* **37**, 6503–6516 (2017).
2. Stokes, M. G. 'Activity-silent' working memory in prefrontal cortex: a dynamic coding framework. *Trends in Cognitive Sciences* **19**, 394–405 (2015).
3. Stokes, M. G. *et al.* Dynamic Coding for Cognitive Control in Prefrontal Cortex. *Neuron* **78**, 364–375 (2013).
4. Wasmuht, D. F., Spaak, E., Buschman, T. J., Miller, E. K. & Stokes, M. G. Intrinsic neuronal dynamics predict distinct functional roles during working memory. *Nat Commun* **9**, 3499 (2018).
5. Kozachkov, L., Lundqvist, M., Slotine, J.-J. & Miller, E. K. Achieving stable dynamics in neural circuits. *PLoS Comput Biol* **16**, e1007659 (2020).
6. Tabareau, N., Slotine, J.-J. & Pham, Q.-C. How Synchronization Protects from Noise. *PLoS Comput Biol* **6**, e1000637 (2010).
7. Börgers, C. & Kopell, N. Synchronization in Networks of Excitatory and Inhibitory Neurons with Sparse, Random Connectivity. *Neural Computation* **15**, 509–538 (2003).
8. Eisen, A. J. *et al. Propofol Anesthesia Destabilizes Neural Dynamics across Cortex*. http://biorxiv.org/lookup/doi/10.1101/2023.11.24.568595 (2023) doi:10.1101/2023.11.24.568595.
9. Denève, S. & Machens, C. K. Efficient codes and balanced networks. *Nat Neurosci* **19**, 375–

382 (2016).

10. Mariño, J. *et al.* Invariant computations in local cortical networks with balanced excitation and inhibition. *Nat Neurosci* **8**, 194–201 (2005).
11. Shu, Y., Hasenstaub, A. & McCormick, D. A. Turning on and off recurrent balanced cortical activity. *Nature* **423**, 288–293 (2003).
12. Ruan, H., Saur, T. & Yao, W.-D. Dopamine-enabled anti-Hebbian timing-dependent plasticity in prefrontal circuitry. *Front. Neural Circuits* **8**, (2014).
13. Turrigiano, G. G. & Nelson, S. B. Homeostatic plasticity in the developing nervous system. *Nat Rev Neurosci* **5**, 97–107 (2004).
14. Sussillo, D. Neural circuits as computational dynamical systems. *Current Opinion in Neurobiology* **25**, 156–163 (2014).
15. Churchland, M. M. *et al.* Neural population dynamics during reaching. *Nature* **487**, 51–56 (2012).
16. Hall, T. M., de Carvalho, F. & Jackson, A. A Common Structure Underlies Low-Frequency Cortical Dynamics in Movement, Sleep, and Sedation. *Neuron* **83**, 1185–1199 (2014).
17. Jiang, X., Saggar, H., Ryu, S. I., Shenoy, K. V. & Kao, J. C. Structure in Neural Activity during Observed and Executed Movements Is Shared at the Neural Population Level, Not in Single Neurons. *Cell Reports* **32**, 108006 (2020).
18. Gao, Y., Archer, E., Paninski, L. & Cunningham, J. P. Linear dynamical neural population models through nonlinear embeddings. (2016) doi:10.48550/ARXIV.1605.08454.
19. Aoi, M. C., Mante, V. & Pillow, J. W. Prefrontal cortex exhibits multidimensional dynamic encoding during decision-making. *Nat Neurosci* **23**, 1410–1420 (2020).
20. Libby, A. & Buschman, T. J. Rotational dynamics reduce interference between sensory and memory representations. *Nat Neurosci* **24**, 715–726 (2021).
21. Mante, V., Sussillo, D., Shenoy, K. V. & Newsome, W. T. Context-dependent computation by recurrent dynamics in prefrontal cortex. *Nature* **503**, 78–84 (2013).

22. Derrfuss, J., Ekman, M., Hanke, M., Tittgemeyer, M. & Fiebach, C. J. Distractor-resistant Short-Term Memory Is Supported by Transient Changes in Neural Stimulus Representations. *Journal of Cognitive Neuroscience* **29**, 1547–1565 (2017).
23. Mallett, R. & Lewis-Peacock, J. A. Working memory prioritization impacts neural recovery from distraction. *Cortex* **121**, 225–238 (2019).
24. Lewis-Peacock, J. A., Drysdale, A. T. & Postle, B. R. Neural Evidence for the Flexible Control of Mental Representations. *Cereb. Cortex* **25**, 3303–3313 (2015).
25. Yoon, J. H., Curtis, C. E. & D'Esposito, M. Differential effects of distraction during working memory on delay-period activity in the prefrontal cortex and the visual association cortex. *NeuroImage* **29**, 1117–1126 (2006).
26. Parthasarathy, A. *et al.* Mixed selectivity morphs population codes in prefrontal cortex. *Nat Neurosci* **20**, 1770–1779 (2017).
27. Suzuki, M. & Gottlieb, J. Distinct neural mechanisms of distractor suppression in the frontal and parietal lobe. *Nat Neurosci* **16**, 98–104 (2013).
28. Brincat, S. L. *et al.* Interhemispheric transfer of working memories. *Neuron* **109**, 1055-1066.e4 (2021).
29. Shinn, M. Phantom oscillations in principal component analysis. *Proc. Natl. Acad. Sci. U.S.A.* **120**, e2311420120 (2023).
30. Muller, L., Chavane, F., Reynolds, J. & Sejnowski, T. J. Cortical travelling waves: mechanisms and computational principles. *Nat Rev Neurosci* **19**, 255–268 (2018).
31. Muller, L. *et al.* Rotating waves during human sleep spindles organize global patterns of activity that repeat precisely through the night. *eLife* **5**, e17267 (2016).
32. Bhattacharya, S., Brincat, S. L., Lundqvist, M. & Miller, E. K. Traveling waves in the prefrontal cortex during working memory. *PLoS Comput Biol* **18**, e1009827 (2022).
33. Bhattacharya, S. *et al.* Propofol Anesthesia Alters Cortical Traveling Waves. *Journal of Cognitive Neuroscience* **34**, 1274–1286 (2022).

34. Davis, Z. W., Muller, L., Martinez-Trujillo, J., Sejnowski, T. & Reynolds, J. H. Spontaneous travelling cortical waves gate perception in behaving primates. *Nature* **587**, 432–436 (2020).
35. Huang, X. *et al.* Spiral Wave Dynamics in Neocortex. *Neuron* **68**, 978–990 (2010).
36. Xu, Y., Long, X., Feng, J. & Gong, P. Interacting spiral wave patterns underlie complex brain dynamics and are related to cognitive processing. *Nat Hum Behav* **7**, 1196–1215 (2023).
37. Buonomano, D. V. & Maass, W. State-dependent computations: spatiotemporal processing in cortical networks. *Nat Rev Neurosci* **10**, 113–125 (2009).
38. Ju, H. & Bassett, D. S. Dynamic representations in networked neural systems. *Nat Neurosci* **23**, 908–917 (2020).
39. Aghagolzadeh, M. & Truccolo, W. Inference and Decoding of Motor Cortex Low-Dimensional Dynamics via Latent State-Space Models. *IEEE Trans. Neural Syst. Rehabil. Eng.* **24**, 272–282 (2016).
40. Diomedi, S., Vaccari, F. E., Galletti, C., Hadjidimitrakis, K. & Fattori, P. Motor-like neural dynamics in two parietal areas during arm reaching. *Progress in Neurobiology* **205**, 102116 (2021).
41. Gallego-Carracedo, C., Perich, M. G., Chowdhury, R. H., Miller, L. E. & Gallego, J. Á. Local field potentials reflect cortical population dynamics in a region-specific and frequency-dependent manner. *eLife* **11**, e73155 (2022).
42. Kalidindi, H. T. *et al.* Rotational dynamics in motor cortex are consistent with a feedback controller. *eLife* **10**, e67256 (2021).
43. Kraus, B. J., Robinson, R. J., White, J. A., Eichenbaum, H. & Hasselmo, M. E. Hippocampal “Time Cells”: Time versus Path Integration. *Neuron* **78**, 1090–1101 (2013).
44. Lara, A. H., Cunningham, J. P. & Churchland, M. M. Different population dynamics in the supplementary motor area and motor cortex during reaching. *Nat Commun* **9**, 2754 (2018).
45. Lebedev, M. A. *et al.* Analysis of neuronal ensemble activity reveals the pitfalls and shortcomings of rotation dynamics. *Sci Rep* **9**, 18978 (2019).

46. Mollazadeh, M., Aggarwal, V., Thakor, N. V. & Schieber, M. H. Principal components of hand kinematics and neurophysiological signals in motor cortex during reach to grasp movements. *Journal of Neurophysiology* **112**, 1857–1870 (2014).
47. Suresh, A. K. *et al.* Neural population dynamics in motor cortex are different for reach and grasp. *eLife* **9**, e58848 (2020).
48. Sussillo, D., Churchland, M. M., Kaufman, M. T. & Shenoy, K. V. A neural network that finds a naturalistic solution for the production of muscle activity. *Nat Neurosci* **18**, 1025–1033 (2015).
49. Gallego, J. A., Perich, M. G., Chowdhury, R. H., Solla, S. A. & Miller, L. E. Long-term stability of cortical population dynamics underlying consistent behavior. *Nat Neurosci* **23**, 260–270 (2020).
50. Kaufman, M. T., Churchland, M. M., Ryu, S. I. & Shenoy, K. V. Cortical activity in the null space: permitting preparation without movement. *Nat Neurosci* **17**, 440–448 (2014).
51. Konecky, R. O., Smith, M. A. & Olson, C. R. Monkey prefrontal neurons during Sternberg task performance: full contents of working memory or most recent item? *Journal of Neurophysiology* **117**, 2269–2281 (2017).
52. Asaad, W. F., Rainer, G. & Miller, E. K. Task-Specific Neural Activity in the Primate Prefrontal Cortex. *Journal of Neurophysiology* **84**, 451–459 (2000).
53. Lundqvist, M. *et al.* Working memory control dynamics follow principles of spatial computing. *Nat Commun* **14**, 1429 (2023).
54. Lundqvist, M., Herman, P. & Lansner, A. Theta and Gamma Power Increases and Alpha/Beta Power Decreases with Memory Load in an Attractor Network Model. *Journal of Cognitive Neuroscience* **23**, 3008–3020 (2011).
55. Lundqvist, M. *et al.* Gamma and Beta Bursts Underlie Working Memory. *Neuron* **90**, 152–164 (2016).
56. Kuzmina, E., Kriukov, D. & Lebedev, M. Neuronal travelling waves explain rotational dynamics in experimental datasets and modelling. *Sci Rep* **14**, 3566 (2024).
57. Benucci, A., Frazor, R. A. & Carandini, M. Standing Waves and Traveling Waves Distinguish

Two Circuits in Visual Cortex. *Neuron* **55**, 103–117 (2007).

58. Roberts, J. A. *et al.* Metastable brain waves. *Nat Commun* **10**, 1056 (2019).
59. Gabay, N. C., Babaie-Janvier, T. & Robinson, P. A. Dynamics of cortical activity eigenmodes including standing, traveling, and rotating waves. *Phys. Rev. E* **98**, 042413 (2018).
60. Goldman, S., Santelmann Jr, W. F., Vivian, W. E. & Goldman, D. Traveling waves in the brain. *Science* **109 (2838)**, 524–524 (1949).
61. Ye, Z. *et al. Brain-Wide Topographic Coordination of Traveling Spiral Waves*. http://biorxiv.org/lookup/doi/10.1101/2023.12.07.570517 (2023) doi:10.1101/2023.12.07.570517.
62. Wang, J., Narain, D., Hosseini, E. A. & Jazayeri, M. Flexible timing by temporal scaling of cortical responses. *Nat Neurosci* **21**, 102–110 (2018).
63. Patel, J., Fujisawa, S., Berényi, A., Royer, S. & Buzsáki, G. Traveling Theta Waves along the Entire Septotemporal Axis of the Hippocampus. *Neuron* **75**, 410–417 (2012).
64. Takahashi, K. *et al.* Large-scale spatiotemporal spike patterning consistent with wave propagation in motor cortex. *Nat Commun* **6**, 7169 (2015).
65. Lubenov, E. V. & Siapas, A. G. Hippocampal theta oscillations are travelling waves. *Nature* **459**, 534–539 (2009).
66. Fries, P. Rhythmic attentional scanning. *Neuron* **111**, 954–970 (2023).
67. Silver, M. A. & Kastner, S. Topographic maps in human frontal and parietal cortex. *Trends in Cognitive Sciences* **13**, 488–495 (2009).
68. Scolari, M., Seidl-Rathkopf, K. N. & Kastner, S. Functions of the human frontoparietal attention network: Evidence from neuroimaging. *Current Opinion in Behavioral Sciences* **1**, 32–39 (2015).
69. Martinius, J. W. & Hoovey, Z. B. Bilateral synchrony of occipital alpha waves, oculomotor activity and “attention” in children. *Electroencephalography and Clinical Neurophysiology* **32**, 349–356 (1972).
70. Hughes, J. R. The Phenomenon of Travelling Waves: A Review. *Clinical*

Electroencephalography **26**, 1–6 (1995).

71. Horn, B. K. P. & Schunck, B. G. Determining optical flow. *Artificial Intelligence* **17**, 185–203 (1981).

72. Townsend, R. G. & Gong, P. Detection and analysis of spatiotemporal patterns in brain activity. *PLoS Comput Biol* **14**, e1006643 (2018).

Acknowledgements

We thank Alex J. Major, Matthew Broschard, Indie C. Garwood, Jefferson Roy, Zhen Chen, Adam Eisen, Alex Bardon, Huidi Li, and Pablo Wentz for their helpful suggestions.

Author contributions

J.A.D., S.L.B., M.L. and E.K.M. designed the experiments. J.A.D. and M.K.M. performed the experiments and recorded the data. S.L.B. curated the data. T.B. and S.L.B. conceived and performed the analysis. E.K.M. supervised the project. T.B., S.L.B. and E.K.M. wrote the manuscript.

Competing interests

The authors declare no competing interests.

Funding

This work was supported by the Office of Naval Research N00014-23-1-2768, The JPB Foundation, The Picower Institute for Learning and Memory (E.K.M.), and ERC starting grant 949131 (M.L.).

Supplementary information

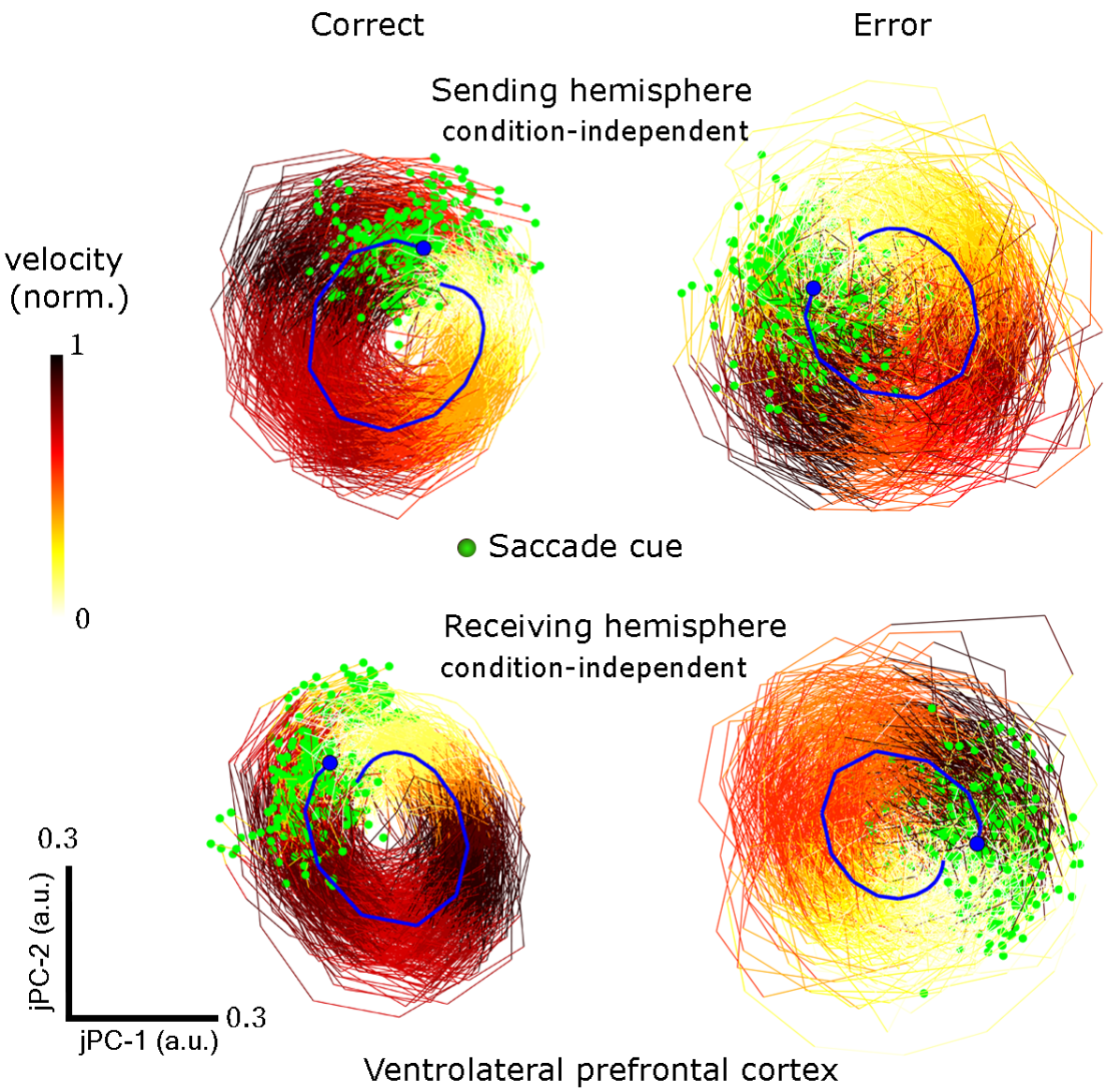

Supplemental Figure 1. Trajectories in the jPC subspace by the spiking data at the ventrolateral prefrontal cortex (vlPFC). On correct trials, the trajectories at the sending hemisphere completed 360 degrees of rotations, and then spiraled to the center (Correct trials, sending hemisphere = 375.03 $\pm$ 7.56 degrees, receiving hemisphere = 363.31 $\pm$ 6.74 degrees; Error trials, sending hemisphere = 341.15 $\pm$ 5.13 degrees, receiving hemisphere = 348.75 $\pm$ 8.16 degrees). We have similar findings at the dorsolateral PFC. The relationship that the trajectories at the sending hemisphere completed more rotations on correct trials than error trials still holds ($P < 0.0001$, one-sided t-test; see also Results section). On correct trials, the trajectories subtended more rotations at the receiving hemisphere of vlPFC than dlPFC ($P = 0.0037$, paired t-test). All stats were presented as mean $\pm$ s.e.m..

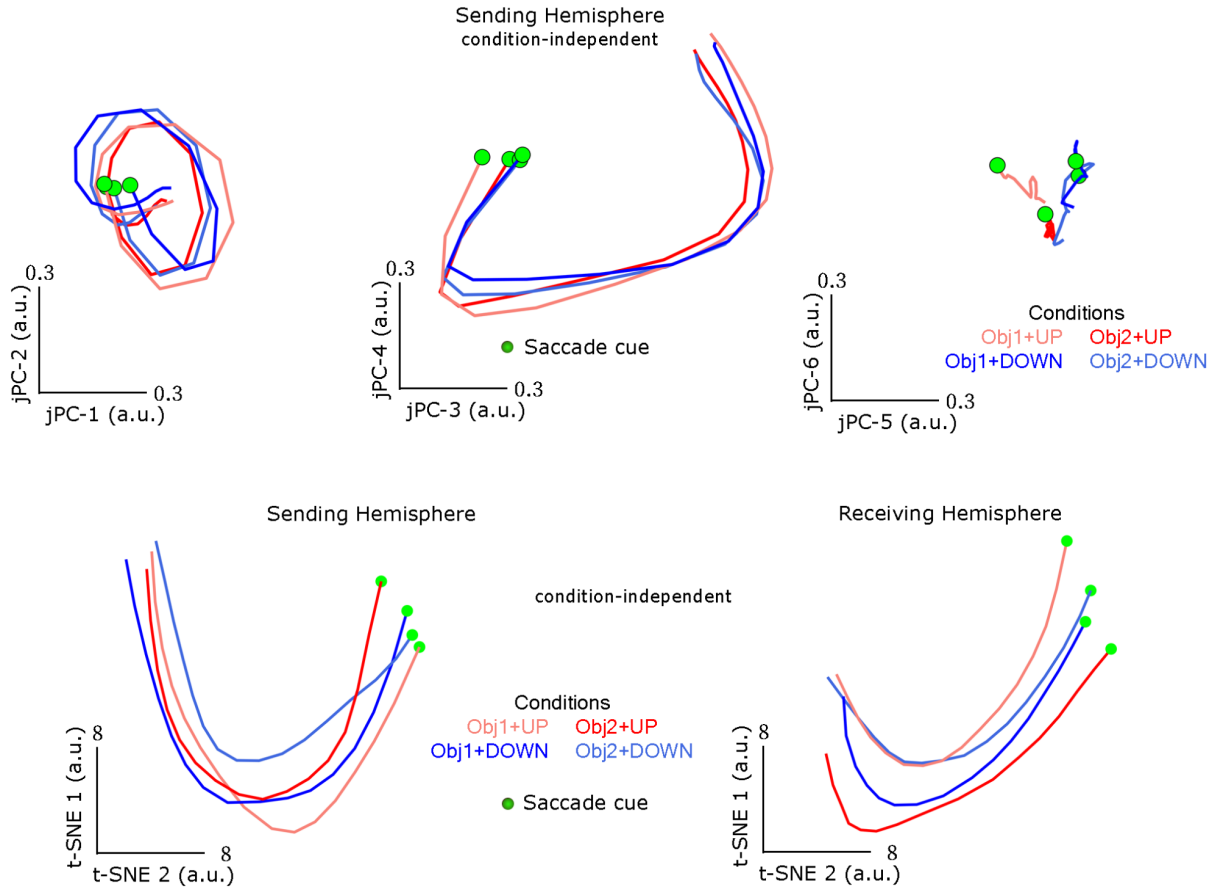

Supplemental Figure 2. (**top row**) Projections of data during post-cue saccade delay of 800 ms on three jPC planes (jPC subspaces). (Left) projections on the top two jPCs, showing rotational trajectories and ordered rotational structures (grouping of trajectories based on the direction of projections and similar angular velocity). This plane contained the fastest angular velocity. (Middle) projections onto the plane of jPC3-4, showing ordered structure but slower angular velocity. The trajectories lost 'circularity' during the middle of the delay, showing relatively 'flat' or linear projections. (Right) projections onto the plane of jPC5-6, showing no rotational trajectories and no rotational structure. (**bottom row**) Projections of spike-rate data on two t-SNE (t-distributed stochastic neighborhood embedding) axes showed rotational trajectories and rotational structures at the sending and receiving hemispheres in one example session by monkey M.

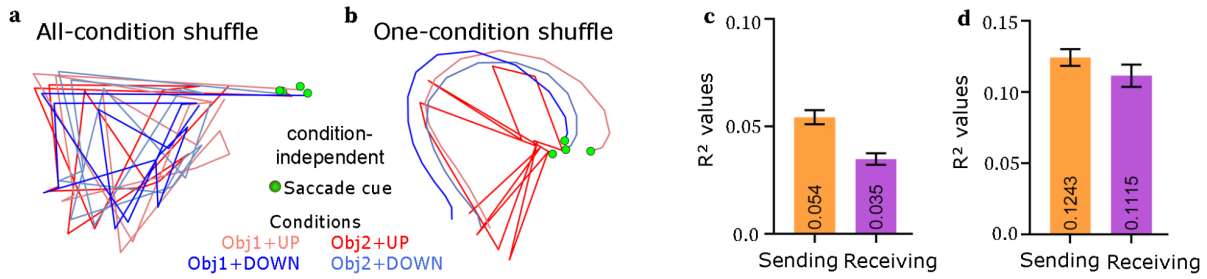

Supplemental Figure 3. (**a**) Trajectories corresponding to four conditions in an example session of saccade-distractor task. Here, time was randomly shuffled in the spiking data of one condition and the data of other conditions were shuffled using the same shuffling order. The rotational structure disappeared, reflected in the poor R^2 values shown in (**c**). (**b**) the data was time shuffled only in one condition (Obj2+UP) in this example. The rotational feature was partly maintained in the conditions where the data were not shuffled. The corresponding R^2 values are shown in (**d**).

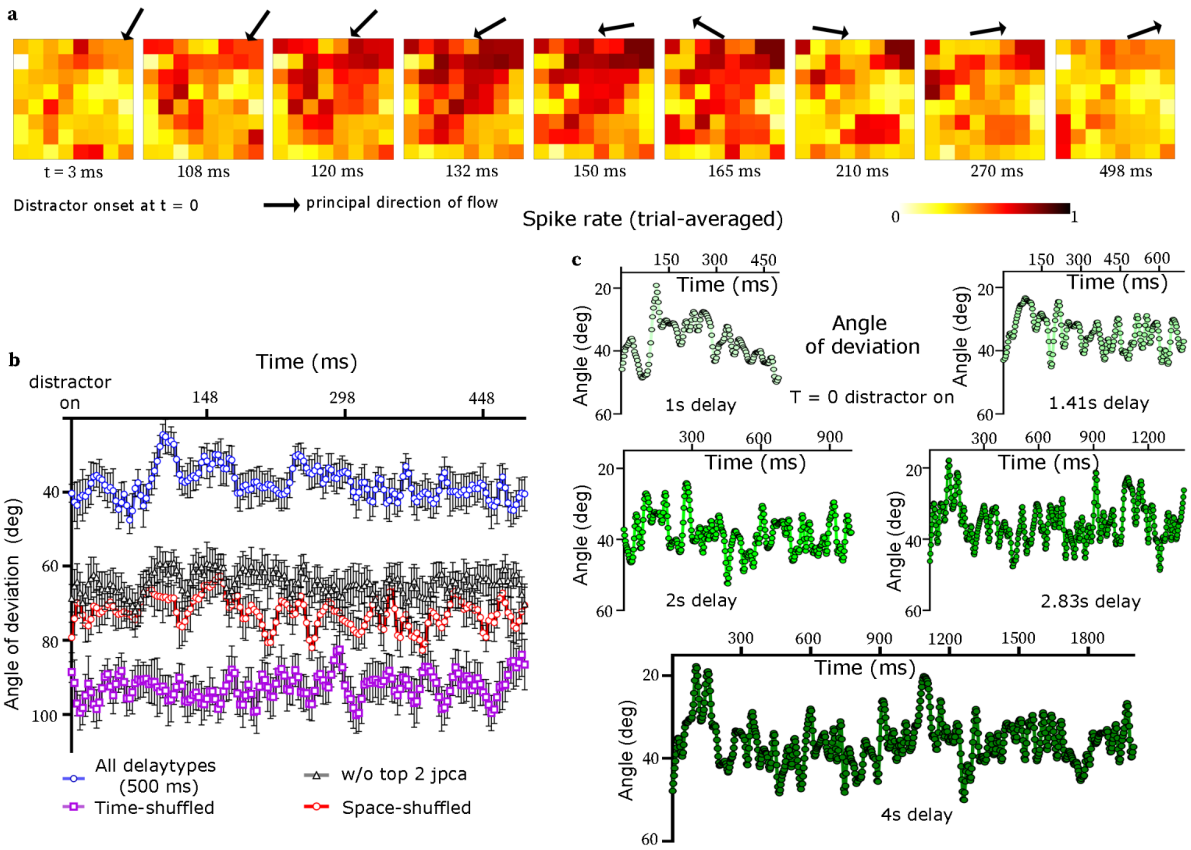

Supplemental Figure 4. Traveling waves by visual distractors. (**a**) A wave of population-level trial-averaged spike-rate caused by a visual distractor (the example was taken from the 1s delay length, and the distractor appeared mid-delay). The principal direction of flow was indicated with black arrows. (**b**) Equivalence between the rotations in the jPC plane and the traveling waves. We used Bonferroni's corrections for multiple comparisons statistical testing. The line in blue shows the change in principal direction of a wave in the spike data. On time-shuffled data (i.e. disrupting the temporal order of the wave), the changes in the principal direction were larger (magenta; $P < 0.0001$, t-test with Welch's correction for variance) compared to the unshuffled data (blue line). On space-shuffled data (i.e. disrupting the spatial order of the wave), the changes were large (red; $P < 0.0001$, t-test with Welch's correction for variance) as well. After deleting the projections on the top two jPCs from the data, the changes (black line) were also higher than the ones in the original data ($P < 0.0001$. paired t-test). This change indicates that the top two jPCs captured an event that had ordered spatiotemporal changes. (**c**) The changes in the principal direction of flow for each delay length.

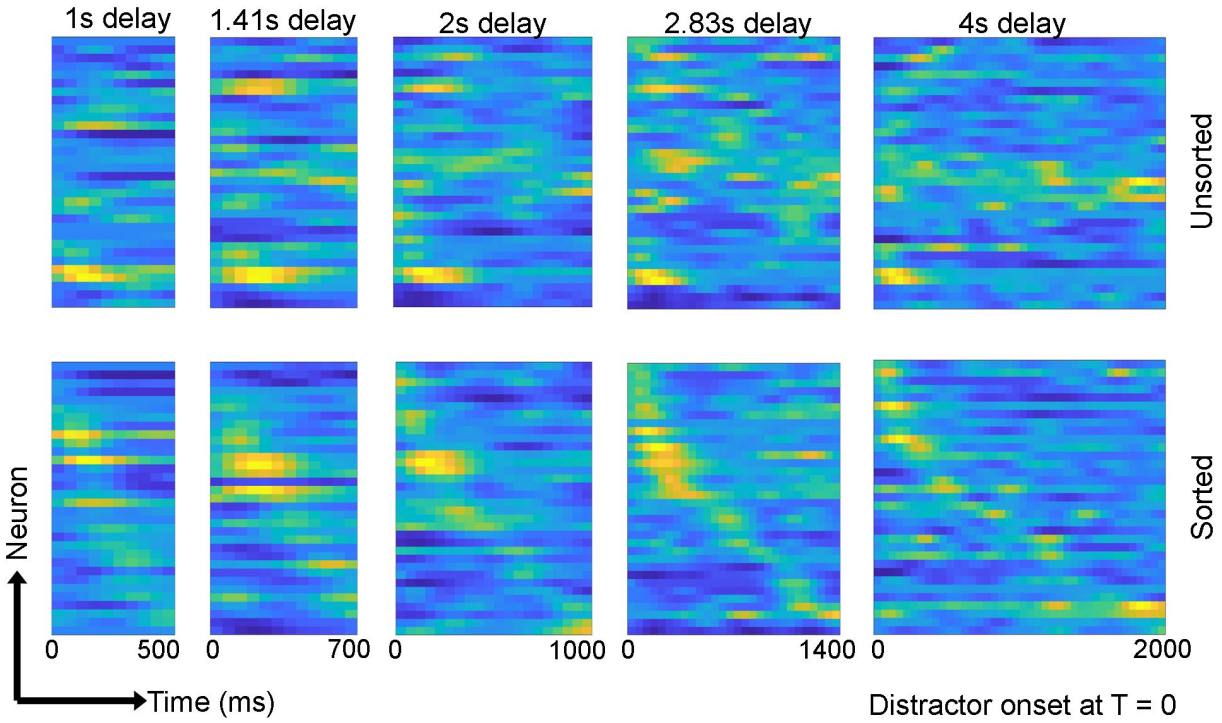

Supplemental Figure 5. Spike-rate data of the visual distractor experiment. (**top panel**) Soft-normalized spike-rate histograms for each delay-type are shown here. The histograms (neuron X time) were taken after the distractor onset, where the onset was at the middle of each delay. (**bottom panel**) Neurons were sorted based on the latency of their peak firing rates. Each histogram exhibited the canonical firing pattern - temporally-graded firing rate, indicative of unique 'population-coding' of the disruption throughout the remainder of each delay.